



Article

# Material Discovery and High Throughput Exploration of Ru Based Catalysts for Low Temperature Ammonia Decomposition

Katherine McCullough , Pei-Hua Chiang, Juan D. Jimenez and Jochen A. Lauterbach \* 

Department of Chemical Engineering, University of South Carolina, Columbia, SC 29208, USA; mccullke@email.sc.edu (K.M.); pchiang@email.sc.edu (P.-H.C.); jiminezj@email.sc.edu (J.D.J.)

\* Correspondence: lauteraj@cec.sc.edu

Received: 21 February 2020; Accepted: 14 April 2020; Published: 16 April 2020



**Abstract:** High throughput experimentation has the capability to generate massive, multidimensional datasets, allowing for the discovery of novel catalytic materials. Here, we show the synthesis and catalytic screening of over 100 unique Ru-Metal-K based bimetallic catalysts for low temperature ammonia decomposition, with a Ru loading between 1–3 wt% Ru and a fixed K loading of 12 wt% K, supported on  $\gamma$ -Al<sub>2</sub>O<sub>3</sub>. Bimetallic catalysts containing Sc, Sr, Hf, Y, Mg, Zr, Ta, or Ca in addition to Ru were found to have excellent ammonia decomposition activity when compared to state-of-the-art catalysts in literature. Furthermore, the Ru content could be reduced to 1 wt% Ru, a factor of four decrease, with the addition of Sr, Y, Zr, or Hf, where these secondary metals have not been previously explored for ammonia decomposition. The bimetallic interactions between Ru and the secondary metal, specifically RuSrK and RuFeK, were investigated in detail to elucidate the reaction kinetics and surface properties of both high and low performing catalysts. The RuSrK catalyst had a turnover frequency of 1.78 s<sup>-1</sup>, while RuFeK had a turnover frequency of only 0.28 s<sup>-1</sup> under identical operating conditions. Based on their apparent activation energies and number of surface sites, the RuSrK had a factor of two lower activation energy than the RuFeK, while also possessing an equivalent number of surface sites, which suggests that the Sr promotes ammonia decomposition in the presence of Ru by modifying the active sites of Ru.

**Keywords:** ammonia decomposition; high throughput; hydrogen production; ruthenium catalyst; promoter; low temperature

## 1. Introduction

Ammonia has proven to be a promising CO<sub>x</sub>-free candidate for hydrogen storage and transportation [1,2]. The main advantages of using ammonia as a hydrogen storage material are its relatively high energy density, existing infrastructure, hydrogen storage capacity, and ability to be liquefied at 293 K and 8 atm of pressure for transportation [1]. Solid hydrogen storage materials, such as metal hydrides and metal organic frameworks, are an attractive alternative, but the release of H<sub>2</sub> from these materials requires harsh operating conditions and often suffers from poor H<sub>2</sub> sorption reversibility [1]. Additionally, these materials have lower hydrogen storage capabilities than ammonia. For example, 10 kg of H<sub>2</sub> can be stored in either 96 kg of liquid ammonia (108 g<sub>H2</sub>/L), 392 kg of Mg<sub>2</sub>NiH<sub>4</sub> (40 g<sub>H2</sub>/L), or 730 kg of LaNi<sub>5</sub>H<sub>6</sub> (36 g<sub>H2</sub>/L) [1,3].

Despite the obvious advantages of H<sub>2</sub> storage through ammonia, on-site power generation via hydrogen fuel cells requires the catalytic decomposition of ammonia, and thus limited by the performance of the catalytic material. This process requires a highly active ammonia decomposition catalyst that can generate H<sub>2</sub> from ammonia at moderate to low temperatures (below 450 °C) in order

to avoid poisoning or degradation of the hydrogen separation membranes, which often exhibit low thermal stability [4]. Supported Ru catalysts are regarded as the most active ammonia decomposition metal and have been studied for over a century. Attempts to utilize lower cost alternatives, such as Fe [5–8], Co [5,9–11], Ni [12–17], Cr [18], and Cu [19] have been demonstrated, but they fail to reach appreciable activity at low temperatures. Their lower apparent activity is attributed to the N<sub>2</sub> binding energy of these metals, as they either bind N<sub>2</sub> too strongly or too weakly to facilitate ammonia decomposition. It is generally accepted that the recombinative desorption of N<sub>2</sub> is the rate determining step for ammonia decomposition [20–23].

Modifications outside the realm of current promotional enhancement is required in order to find a low cost, low temperature ammonia decomposition catalyst. A number of studies continue to focus on the optimization of Ru based systems. This is typically achieved by providing electronic modification with the addition of alkali and alkaline earth metals, specifically K, Cs, and Ba [24–28], or by manipulating the dispersion and size of Ru particles [29–31], thus taking advantage of the structure sensitive nature of the reaction. Additionally, using highly basic support materials provides further electronic modification to the catalyst [32–36]. Intelligent design and theoretical investigations of novel bimetallic catalysts for ammonia decomposition are most frequently based on calculated N<sub>2</sub> binding energies. Thus, bimetallic catalysts have been created by taking one metal with a higher binding energy than Ru and another with lower binding energy, so that the linear combination of the two produces a catalyst with a similar binding energy to Ru. This has been demonstrated with Co-Mo [37–39], Fe-Co [40] and Ni-Fe [41] alloys and bimetallic catalysts. However, these bimetallic catalysts are not able to achieve activity within the low temperature ranges that are needed for PEM fuel cells and were significantly outperformed by Ru based catalysts.

Being motivated by the lack of compositional diversity in this field, we sought to perform a comprehensive screening for ammonia decomposition catalysts with the aim to discover new catalyst compositions, reduce Ru content, and obtain near thermodynamic ammonia conversion at temperatures at or below 400 °C under realistic operating conditions. A catalyst containing 4 wt% Ru promoted by 12 wt% K supported on gamma-alumina was used as a base catalyst composition, and was systematically modified by substituting Ru with different alkaline earth metals, transition metals, noble metals, and metalloids. These include Mg, Ca, Sr, Sc, Y, Zr, Hf, Nb, Ta, Cr, Mo, W, Mn, Re, Fe, Os, Co, Rh, Ir, Ni, Pd, Pt, Cu, Ag, Au, Zn, Cd, In, Sn, Pb, and Bi. In this way, we were able to study trends in activity as the ratio of Ru metal to the substituted metal decreased from 3:1 to 2:2 to 1:3. In total, 33 different metals and 94 unique catalyst formulations were synthesized and then tested for their low temperature ammonia decomposition activity using a 16-channel parallel high throughput reactor system. Catalysts containing Hf, Y, Sc, Sr, Mg, Zr, Ta, and Ca were able to achieve high activity with less Ru. Additionally, the Sr, Y, Zr, and Hf catalysts were able to achieve greater than 80% conversion at 400 °C with as little as 1% Ru. To the best of our knowledge, these catalyst materials have not been previously reported. In this work, we investigated the kinetics and adsorption properties of these Ru based Sr and Fe containing catalysts to understand the effect that secondary metal substitution has on activity.

## 2. Materials and Methods

### 2.1. Catalyst Synthesis

The catalysts were synthesized using the incipient wetness impregnation technique and were supported on SBA-200  $\gamma$ -Al<sub>2</sub>O<sub>3</sub> (Catalox, 99.99%, 192 ± 20 m<sup>2</sup>/g, 30 Å pore radius, 0.45 mL/g pore volume), where the support materials was used as received from the manufacturer. KCH<sub>3</sub>COO (Fischer Scientific, Waltham, MA, USA, 98% purity), anhydrous RuCl<sub>3</sub>, and anhydrous chloride salts of the following: Mg, Ca, Sr, Sc, Y, Zr, Hf, Nb, Ta, Cr, Mo, W, Mn, Re, Fe, Os, Co, Rh, Ir, Ni, Pd, Pt, Cu, Ag, Au, Zn, Cd, In, Sn, Pb, and Bi (Sigma Aldrich, ≥ 95% purity) were used without further modification. The support was first dried at 120 °C for 2 h before impregnation. An appropriate amount of RuCl<sub>3</sub>,

secondary anhydrous chloride salt, and  $\text{KCH}_3\text{COO}$  were mixed to obtain 3:1:12, 2:2:12, or 1:3:12 weight ratios of Ru:M:K (where M = Mg, Ca, Sr, Sc, Y, Zr, Hf, Nb, Ta, Cr, Mo, W, Mn, Re, Fe, Os, Co, Rh, Ir Ni, Pd, Pt Cu, Ag, Au, Zn, Cd, In, Sn, Pb, or Bi) and dissolved in DI water. An aliquot of solution was then added to the dried support under magnetic stirring until incipient wetness was achieved. The impregnated support was then dried at 120 °C for 30 min., after which the process was repeated until the entire solution was impregnated onto the support. The catalysts were then ground and heated at 200 °C for 2 h, and subsequently calcined in air at 550 °C for 3 h.

## 2.2. Catalytic Performance

### 2.2.1. High-Throughput Screening

Catalytic testing was carried out in a 16-channel parallel reactor system. The temperature of each of each of the 16 catalyst beds was measured using K-type thermocouples. The gas effluent of the reactor system was analyzed using a Bruker Equinox 55 FT-IR spectrometer (Bruker, Billerica, MA, USA) coupled with a  $128 \times 128$ -pixel mercury cadmium telluride (MCT) focal plane array. Further details of the system along with a reactor schematic can be found elsewhere [42,43]. Various known concentrations of  $\text{NH}_3$  were flown through the empty reactor channels and their IR spectra were acquired for each reactor channel in order to quantify the effluent stream. The integrated peak area was used to correlate the IR signal with  $\text{NH}_3$  concentration using GRAMS AI software (version 9.3, ThermoFischer, Waltham, MA, USA). The catalysts were first heated to 450 °C under Ar followed by a reduction in 10%  $\text{H}_2$  for 1 h. Catalyst activity was screened while using 200 mg of catalyst and at a space velocity of 30,000 mL/hr/g<sub>cat</sub> under 1%  $\text{NH}_3$  in balance Ar and at atmospheric pressure. Measurements were taken in 50 °C increments from 250 °C to 400 °C.

### 2.2.2. Catalyst Activity under Pure Ammonia

The catalysts were run under pure  $\text{NH}_3$  (99.995%, Airgas) in order to measure catalytic activity, activation energies under differential conditions (2–12% conversion) and the turnover frequency (TOF) at 300 °C, 350 °C and 400 °C. A single channel plug flow reactor was used where the catalysts was supported in the center of the furnace using quartz wool and a supporting rod. The flowrates were controlled using Brooks Mass Flow Controllers (Brooks Instrument, Hatfield, PA, USA). Catalysts were first heated to 450 °C in Ar and then subjected to a 10%  $\text{H}_2$  reduction for one hour. For catalyst activity,  $\text{NH}_3$  conversion was then measured in 50 °C increments from 250 °C to 400 °C. The catalyst bed temperature was measured using a K-type thermocouple and the space velocity was kept constant for each reaction at  $5400 \text{ mL}_{\text{NH}_3} \text{ hr}^{-1} \text{ g-cat}^{-1}$  using 500 mg of catalyst. The thermodynamic equilibrium calculations for ammonia decomposition at 1 bar may be found in Figure S1. The product stream was analyzed using a Shimadzu 2014 gas chromatogram (Shimadzu, Kyoto, Japan) that was equipped with a thermal conductivity detector (TCD). The GC is equipped with a Mol Sieve 5A plot column for  $\text{H}_2$  and  $\text{N}_2$  separation. The concentration of  $\text{H}_2$  and  $\text{N}_2$  in the product stream were used to calculate the  $\text{NH}_3$  conversion at each temperature and they were always found to be in stoichiometric proportions.  $\text{NH}_3$  conversion using pure  $\gamma\text{-Al}_2\text{O}_3$  was first measured under these conditions and found to be negligible at all temperatures. The activation energy measurements were carried out twice for each catalyst, and the average activation energy and standard deviation is reported.

## 2.3. Catalyst Characterization

X-ray diffraction (XRD) was carried out to determine the structural composition of the active catalyst components. XRD was carried out for all of the samples in a Rigaku Miniflex II (Tokyo, Japan) that was equipped with a Cu-K $\alpha$  X-ray source and a high-speed silicon-strip detector. The scans were completed between a 10 and 80° 2 $\theta$  angle at a rate of 2°/min. with step size of 0.02°. Hydrogen chemisorption was conducted on a Micromeritics Autochem II 2920 (Micromeritics, Norcross, GA, USA) equipped with a TCD, in order to determine the number of exposed Ru surface atoms per gram of Ru. Catalysts were first

reduced at 450 °C in 10% H<sub>2</sub>/Ar and then heated to 460 °C for 15 min under inert gas to remove excess H<sub>2</sub> from the surface. The catalysts were then cooled to 50 °C, and a 10% H<sub>2</sub>/Ar mixture was pulsed, and the amount of H<sub>2</sub> adsorbed was determined. The turnover frequencies were calculated assuming a H<sub>2</sub>:Ru ratio of 1:1 [44]. CO adsorption was performed via diffuse reflectance IR spectroscopy while using a Bruker Vertex 70 FT-IR spectrometer (Bruker, Billerica, MA, USA) equipped with an MCT detector cooled by liquid nitrogen and a Praying Mantis Diffuse Reflectance cell (Harrick Scientific Products, Pleasantville, NY, USA). The spectra were taken with a resolution of 4 cm<sup>-1</sup> and averaged over 512 scans. The catalysts were first heated to 450 °C under N<sub>2</sub> (UHP, Airgas), and then subjected to a 10% H<sub>2</sub> pretreatment for one hour. The catalysts were then cooled to 50 °C under inert, and a mixture gas of 1000 ppm CO in balance He was used for room temperature CO adsorption. The SEM images were taken on a Zeiss Ultra Plus FESEM (Carl Zeiss, Oberkochen, Germany) and TEM images were taken on a Hitachi HT7800 TEM (Hitachi, Tokyo, Japan).

### 3. Results and Discussion

#### 3.1. Design Space for the Initial High Throughput Screening

Previous work from our group utilized a response surface methodology to optimize the promoter elements and weight loading for a Ru based catalyst for ammonia decomposition, where the optimal promoter element and loading for 4 wt% Ru/ $\gamma$ -Al<sub>2</sub>O<sub>3</sub> was found to be 12 wt% K [45]. The resultant 4%Ru-12%K/ $\gamma$ -Al<sub>2</sub>O<sub>3</sub> catalyst was chosen as the starting point for our initial high throughput study. The Ru content was then reduced and substituted with different elements in order to determine to what extent the replacement of Ru with a secondary element can be modified. The total metal weight loading was kept constant at 4% for all catalysts in order to isolate the influence of the secondary element. The Ru content was reduced by either 1%, 2%, or 3% and substituted with either Mg, Ca, Sr, Sc, Y, Zr, Hf, Nb, Ta, Cr, Mo, W, Mn, Re, Fe, Os, Co, Rh, Ir, Ni, Pd, Pt, Cu, Ag, Au, Zn, Cd, In, Sn, Pb, or Bi, so that the total metal weight loading sums to 4%. This resulted in three different catalyst formulations for each of the 31 elements studied. The ratio of Ru metal to secondary metal was 3:1, 2:2, or 1:3. Each catalyst was promoted with 12% K and supported on  $\gamma$ -Al<sub>2</sub>O<sub>3</sub>. For example, a catalyst containing 3% Ru, 1% Fe, and 12%K, and supported on  $\gamma$ -Al<sub>2</sub>O<sub>3</sub> will be referred to as 3,1,12 RuFeK, and this nomenclature will be used for all catalysts and weight loadings.

It is worth noting that the K promotion and weight loading used will not be at an optimum for all Ru substituted catalysts studied. However, we can ensure that changes in reaction order will be due to the substituted secondary metal by using the same promoter/support combination throughout the study, and not due to newly introduced promoter support interactions, which is beyond the scope of this work. Additionally, because the support material is also kept constant, we can ensure that the interaction between the promoter and the support material is consistent across each catalyst, as different promoters will exhibit different modification effects, depending on the support used [26,46,47]. The same support utilized in the original response surface study mentioned previously was applied herein because of the dependency of the support on the effect of promoter modification.

#### Characterization of 4 Ru/Al<sub>2</sub>O<sub>3</sub> and 4,12 RuK/Al<sub>2</sub>O<sub>3</sub> Baseline Catalysts

A baseline catalyst containing 4 wt% Ru and 12% K supported on  $\gamma$ -Al<sub>2</sub>O<sub>3</sub> was first synthesized in order to make effective comparisons of the substituted Ru catalyst, as described elsewhere [45]. Figure 1a,b show the SEM and TEM image of the unpromoted baseline catalyst and Figure 1c,d show the SEM and TEM image of the 4,12 RuK catalyst. It is apparent from the SEM and TEM analysis that the addition of K influences the Ru morphology on the catalyst surface, which correlates to the KRu<sub>4</sub>O<sub>8</sub> hollandite structure [45]. The hollandite structure is a one-dimensional material that consists of edge sharing RuO<sub>6</sub> octahedrons that share corner oxygens with adjoining octahedrons, thus forming 2 × 2 square tunnels, which contain K cations [48–50]. This structure can be observed in both the SEM



and TEM images of the 4,12 RuK catalyst. Figure 1e,f show the XRD patterns for the unpromoted 4 wt% Ru catalyst (4 Ru) and the baseline K promoted Ru catalyst (4,12 RuK).

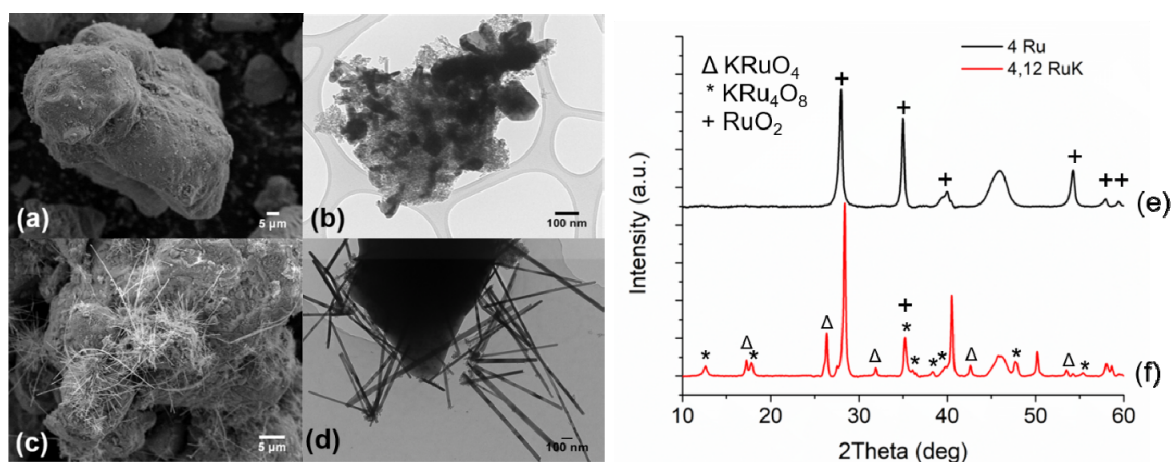


**Figure 1.** Left panel: SEM images of (a) 4 Ru/Al<sub>2</sub>O<sub>3</sub> and (c) 4,12 RuK/Al<sub>2</sub>O<sub>3</sub>. TEM images of (b) 4 Ru/Al<sub>2</sub>O<sub>3</sub> and (d) 4,12 RuK/Al<sub>2</sub>O<sub>3</sub>. Right panel: corresponding XRD patterns of (e) 4 Ru/Al<sub>2</sub>O<sub>3</sub> and (f) 4,12 Ru/Al<sub>2</sub>O<sub>3</sub>.

In both XRD patterns, amorphous Al<sub>2</sub>O<sub>3</sub> is apparent at around 46°. The unpromoted 4 wt% Ru catalysts forms large RuO<sub>2</sub> domains, corresponding to reflections positioned at 28°, 35°, 40°, 57.9°, and 59.4° [51,52]. The size of these domains, calculated via Scherrer's Equation, is roughly 23.1 nm. The 4,12 RuK includes several additional reflections. First, crystalline KCl is apparent at 28.33°, 40.5°, 50.1°, and 58.6° (not labeled for clarity). The slight shoulder on the left of the KCl reflection at 28° indicates that there are small amounts of RuO<sub>2</sub> present in the 4,12 RuK catalyst. New phases appear at 17.2°, 26.3°, 42.5°, and 53.5° that correspond to KRuO<sub>4</sub> [53,54], with an average domain size of 29.8 nm. Additionally, the reflections that appear at 12.6°, 17.8°, and 35.1° correspond to the hollandite phase KRu<sub>4</sub>O<sub>8</sub> [48,54], with an average crystallite size of 17.8 nm.

The catalysts with the Ru based hollandite structure present before reaction were previously found to have increased low temperature ammonia decomposition activity [30], although polycrystalline hollandite and its use as a catalytic material is not well understood. Here, Ru is found in the 3<sup>+</sup>/4<sup>+</sup> oxidation state. One reason for the increased activity of KRu<sub>4</sub>O<sub>8</sub> over RuO<sub>2</sub> nanoparticles might be due to the intimate positioning of K and Ru in these structures. In this way, the catalyst shows increased activity due to electron donation. Additionally, KRu<sub>4</sub>O<sub>8</sub> can act as a precursor for disordered Ru<sup>0</sup> structures, which result in the formation of crystal defects that could greatly enhance the intrinsic activity of Ru based catalysts, where an increase in the defect density on Ru has been shown to greatly improve catalytic performance [22,55].

### 3.2. High-Throughput Screening of Ru Based Catalysts

The K promoted Ru based catalysts with metal substitution were screened for ammonia decomposition activity in 1% NH<sub>3</sub>/Ar at 30,000 mL/hr/g<sub>cat</sub>, where Figure 2 shows the results of the screen at 300 °C. The horizontal dashed line corresponds to the activity of the baseline 4,12 RuK catalyst. Figures S2–S4 show the catalytic activity of all compositions at 250 °C, 350 °C, and 400 °C. Catalytic performance at 300 °C was used to determine the successful catalysts from the screen, due to the large range of responses exhibited, and in the interest of finding substitutional materials that exhibit low temperature activity. Catalyst compositions exceeding the activity of the promoted baseline catalyst (4,12 RuK) are considered to be successful. Due to the complex relationship present in these catalysts, a general discussion of trends will be given herein, followed by a more in-depth comparison between the Sr and Fe containing catalysts.

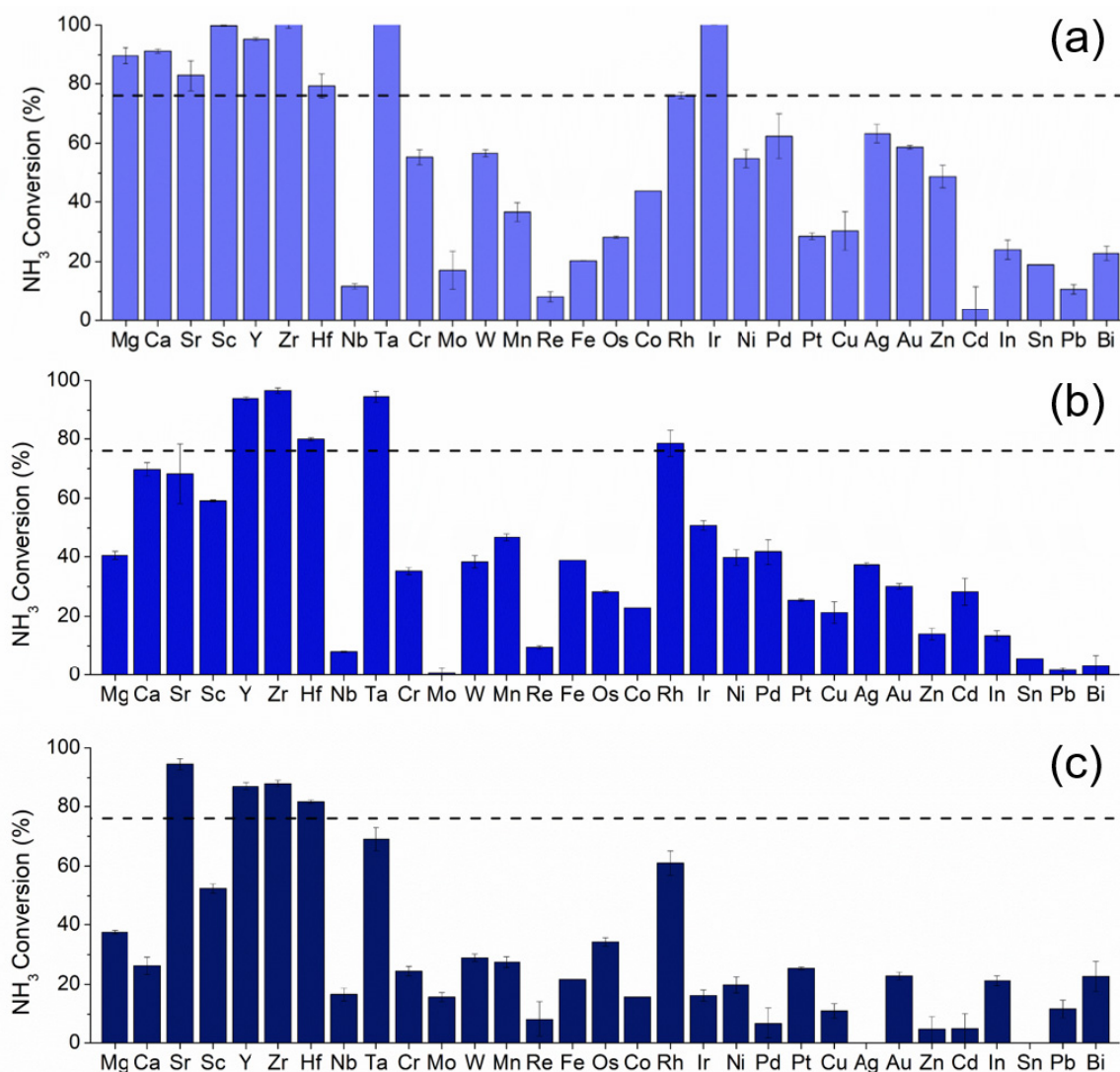


**Figure 2.** Catalytic activity at 300 °C of (a) 3,1,12 RuMK, (b) 2,2,12 RuMK, and (c) 1,3,12 RuMK, where the secondary metal M, is listed on the x-axis. The black dashed line indicates the activity of the baseline 4,12 RuK catalyst at 300 °C. Reaction conditions: 1% NH<sub>3</sub>/Ar, 1.01 bar, 30,000 mL/hr/g<sub>cat</sub>.

The crystalline structure of the entire catalyst library was probed via XRD in order to determine the phases of Ru present and whether secondary phase formation occurred with the addition of a secondary metal. The complete XRD analysis of all the materials can be found in the Supplemental Information (Figures S6–S32). Catalysts containing 3% Ru (Figure 2a) and 1% of Mg, Sr, Ca, Hf, Sc, Ta, Zr, Ir, or Y achieved greater than 83% conversion at 300 °C. As the loading of Ru decreased to 2% (Figure 2b), the activity of Mg, Sc, and Ca containing catalysts declined, while Y, Zr, Sr, Hf, and now Rh, continued to exhibit high performance. With the further decrease to 1% Ru (Figure 2c), only Sr, Y, Zr, and Hf substitution continued to remain highly active. In contrast, Bi, In, Mo, Nb, Cu, Re, Cd, Sn, and Pb lowered the catalytic performance, independent of the Ru loading. This might be due to the poor electronegativity and electron withdrawing nature of these elements, as previous studies have shown that dopants and supports with strong basicity and electrical conductance greatly enhance activity [56–60]. For example, small amounts of Nb have been shown to drastically increase the number of Lewis acid sites present in bulk Ni-Nb-O mixed metal oxides, and thus the enhanced acidity may be responsible for the poor activity seen here [61].

While catalysts containing 3% Ru and 1% Mg, Sr, Ca, Sc, or Y outperformed the baseline 4,12 RuK composition at 300 °C, as the ratio of Ru to secondary metal was further decreased, the activity of

Mg, Sc, and Ca containing catalysts drastically declined, while the Y and Sr catalysts remained highly active with as low as 1% Ru. While alkali metals are regarded as electronic promoters, Mg and Ca are usually considered to be structural promoters [28,29]. Thus, while Mg and Ca may act to increase the number of active sites present on the catalyst, the intrinsic rate of these sites would not be modified [62]. Therefore, as the Ru loading decreases, the number of active sites present would also decrease with the addition of Mg and Ca.

The substitution of Ru with transition metals, primarily Group V–VII, generally resulted in a catalyst with poorer activity than the baseline catalyst. As the Ru loading continued to decrease from 3 wt% (Figure 2a) to 1 wt% (Figure 2c), there is an observed decline in activity that remains relatively constant, regardless of the catalyst composition. Ru active sites are being replaced with different sites that are intrinsically less active than Ru, as Ru is substituted with transition metals [23,37,63]. Therefore, the active sites of Ru are not being structurally or electronically modified, but simply replaced with those with lower rates of reaction or that hinder the rate determining step of the recombination and desorption of N<sub>2</sub>. The activity of the noble metal substituted catalysts showed a higher sensitivity to the variation in weight loadings, and a decrease in activity is observed with increasing noble metal loading. One reason for this observation might be due to the inhibitive effect of hydrogen on the reaction rate over Ru [26,64]. While small additions of noble metals can act as a promoter, larger relative loadings would thus result in a higher degree of inhibition due to the hydrogen spillover effect exhibited by these noble metals, such as Pt and Pd [65–68].

The activity of other monometallic catalysts for ammonia decomposition generally follows: Ru > Rh > Ni > Co > Ir > Fe >> Pt > Cr > Pd > Cu >> Pb [69]. The activity of the catalysts studied here do indeed follow the observed trend in activity of Rh > Ni > Co > Fe > Pt > Cr > Pd. Therefore, in general, we can conclude that the addition of Group V–VII transition metals ultimately did not result in any positive interactions between Ru and the substituted metal, due to the activity following the general trends of the monometallic metals that has already been established in the literature. It might then follow that the metals on the surface may be isolated from each other and not in intimate contact. Based on the summary of the crystalline structure and the catalytic performance, we are attributing the presence of KRuO<sub>4</sub> and KRu<sub>4</sub>O<sub>8</sub> to increased catalytic activity. However, we were not able to definitively correlate this claim due to the complexity of these structures and the difficulty of isolating these phases while also adding a secondary metal to the catalyst. Therefore, a detailed crystallographic study on the effects of phase on catalytic performance using *in situ* XRD and *in situ* electron microscopy would be of great interest, but outside the scope of this work.

Due to the complex relationships present in these multicomponent catalysts, a random forest machine learning algorithm was recently applied to a subset of the data shown here in order to determine what material properties led to catalysts with high activity [57]. While previous work has looked at single variables to describe the trends exhibited by metals for ammonia decomposition, no single variable has been able to correctly predict the trends across a variety of metals [63]. However, looking at two-way interactions between features provides new insight into the relationships between electronic characteristics and catalyst activity. For example, Figure 3 shows the relationship between activity and the mean absolute deviation (MAD) of the catalyst work function and the MAD of the number of d-shell valence electrons. It is apparent that catalysts with lower work function and a lower number of d-shell valence electrons resulted in a higher activity catalyst.

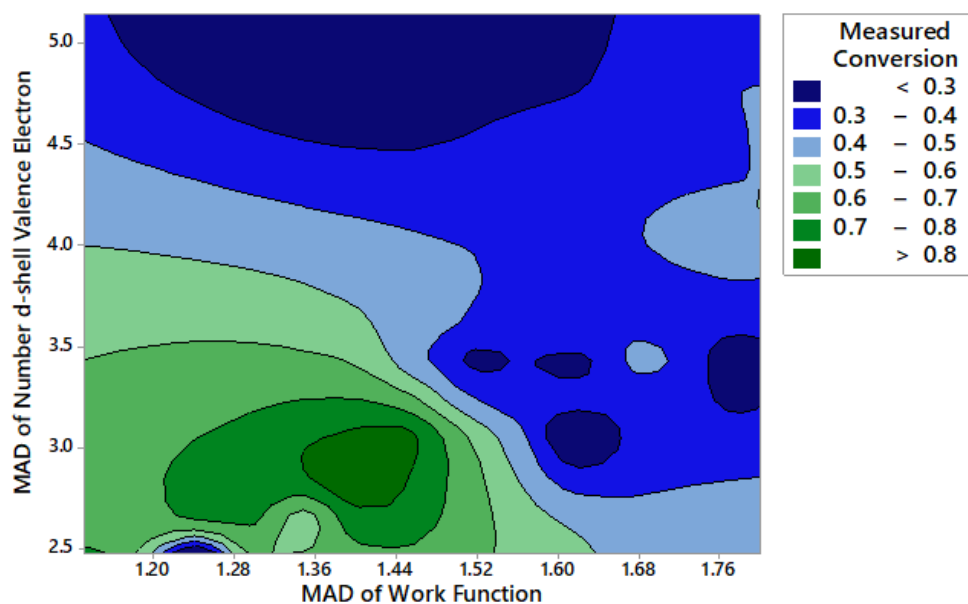


**Figure 3.** Ammonia decomposition activity at 300 °C as a function of the mean absolute deviation (MAD) of the number of d-shell valence electrons and the MAD of the catalyst work function.

In general, it was determined that the number of d-shell valence electrons, electronegativity, covalent radius, and work function all played an important role in determining the catalytic activity. These additional features are related to the electronic characteristics of the catalyst, where the electronic structure of the catalyst has been known to influence the strength of the bond between the metal surface and adsorbate, which affects the activity and reactivity of the catalyst [70,71]. Therefore, we further investigated the influence of highly active Sr and less active Fe catalysts on ammonia decomposition activity, and whether or not surface modification played an important role in activity.

### 3.3. Influence of Sr and Fe on $\text{NH}_3$ Decomposition Activity and Kinetics

The addition of Sr to the Ru based catalysts showed that the Ru content could be reduced to 1% and still maintain high activity at 300 °C. While Mg, Ca, and Ba are often used in ammonia synthesis and decomposition for their excellent promotional abilities, there is little information on the other alkaline earth metal Sr, and its utilization in this reaction. Additionally, Fe is commonly used as an alternative to Ru for both ammonia synthesis and decomposition. However, we observed poor activity across all three weight loadings of Fe based catalysts. For these reasons, Sr and Fe were chosen to discern the trends in catalytic performance under higher ammonia feed gas concentrations to ultimately elucidate the reaction kinetics and surface properties of both high and low performing catalysts for ammonia decomposition.

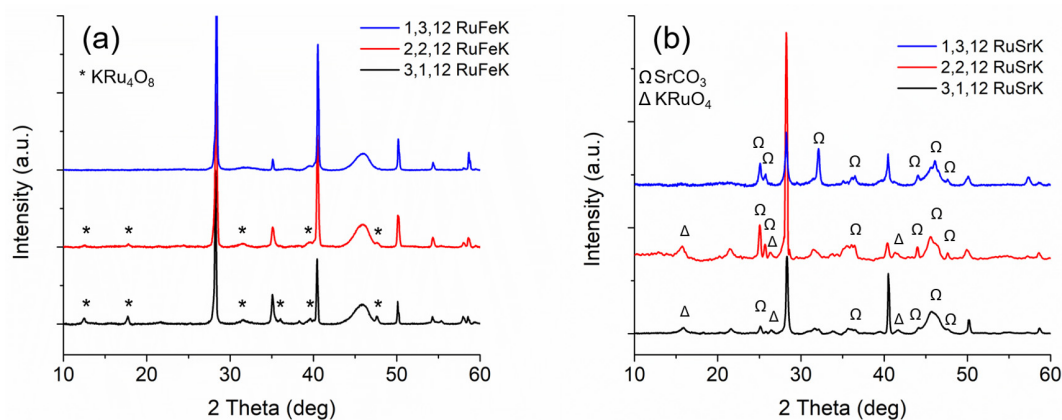
#### 3.3.1. Characterization of Sr and Fe Catalysts

Figure 4a,b show the XRD patterns for each of each weight loading of the Fe and Sr catalysts, respectively.

Fe containing catalysts contain sharp reflections at 28.33°, 40.5°, 50.1°, and 58.6°, which are indicative of KCl formation. The Fe catalysts primarily form crystalline  $\text{KRu}_4\text{O}_8$ , and decrease in relative intensity with decreased Ru loading, such that there are no Ru phases present in the 1,3,12 RuFeK, which indicates highly dispersed hollandite. No Fe phases were present, suggesting either the formation of amorphous Fe species or highly dispersed oxide species. In contrast, the Sr catalysts formed  $\text{KRuO}_4$  indicated by reflections at 17.2°, 26.3°, and 42.5° [53,54].  $\text{SrCO}_3$  is present in all three Sr catalysts and increases in the relative intensity with decreasing Ru loading. Additionally, the relative intensity of KCl varied as the weight loading of Sr and Ru varied, which suggested that there might be more free



Cl ions on the surface of the catalyst, or that an X-ray amorphous Sr oxo-chloro complex may have formed. Additionally, we observe strong K modification to the  $\text{Al}_2\text{O}_3$  surface, which is evidenced by new reflections appearing at ca.  $24.1^\circ$  [72].



**Figure 4.** (a) XRD patterns of (from top to bottom): 1,3,12 RuFeK, 2,2,12 RuFeK and 3,1,12 RuFeK. (b) XRD patterns of (from top to bottom): 1,3,12 RuSrK, 2,2,12 RuSrK, and 3,1,12 RuSrK.

Figure 5a shows a SEM image of the 1,3,12 RuFeK catalyst and Figure 5c shows the corresponding TEM image. Very small rod like particles are visible on the peripheral surface of the  $\text{Al}_2\text{O}_3$ , which confirm highly dispersed  $\text{KRU}_4\text{O}_8$ . Figure 5b,d show the SEM and TEM image of the 1,3,12 RuSrK, respectively. Figure 5d shows the  $\text{KRUO}_4$  complex, which exhibits a narrow, thin sheet-like structure, in contrast to the stiff rod-like structure that is exhibited by hollandite in Figure 1b.

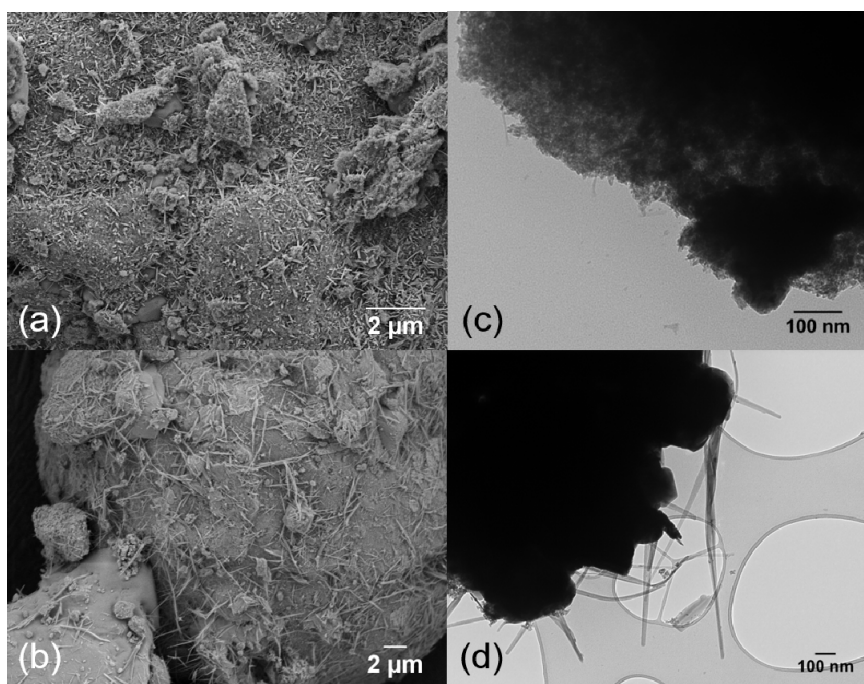


**Figure 5.** (a) SEM image and (c) TEM image of 1,3,12 RuFeK. (b) SEM image and (d) TEM images of 1,3,12 RuSrK.

### 3.3.2. Evaluation of Apparent Activation Energy and TOF

The apparent activation energies were calculated for each of the three weight ratios of the Fe and Sr catalysts, for a total of six catalysts. The Arrhenius plots for are shown for the Sr and Fe in Figure 6a,b, respectively. The activation energies were calculated under differential conditions in 100%  $\text{NH}_3$  and

at 5400 mL/hr/g<sub>cat</sub>. The Weisz–Prater criterion was used to determine the absence of internal mass transfer resistances [73,74] (see Supplemental Information), and no mass transfer limitations were observed. Figure S5 shows the Arrhenius plots for the 4 Ru and 4,12 RuK catalysts.

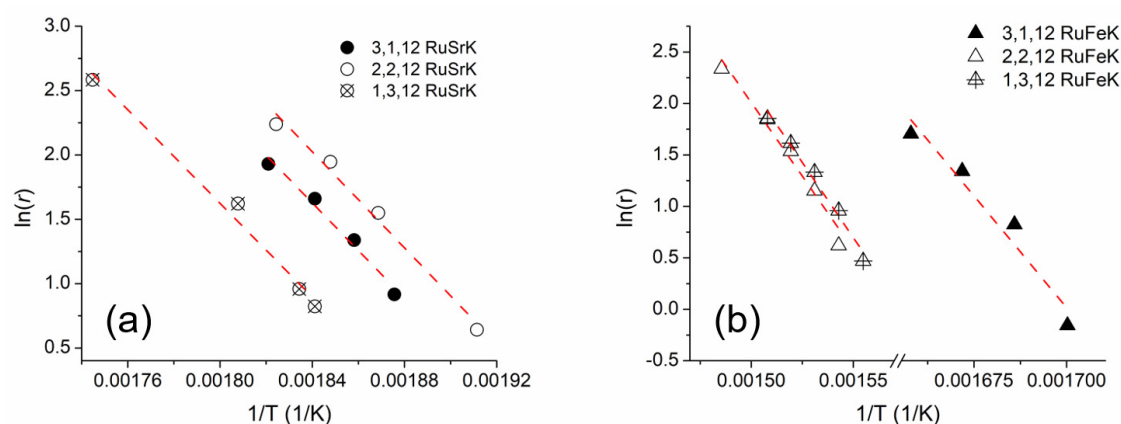


**Figure 6.** Arrhenius plot of (a) RuSrK and (b) RuFeK based catalysts. Reaction Conditions: 100% NH<sub>3</sub>, 5400 mL/hr/g<sub>cat</sub> and 1 bar. Apparent activation energies were conducted under differential conditions.

Additionally, the turnover frequency (TOF) for each substituted Ru catalyst was determined and compared to the 4,12 RuK and unpromoted 4 Ru catalysts. The TOF was calculated by normalizing the rate of reaction to the number of exposed Ru atoms per gram of Ru, which were determined via H<sub>2</sub> chemisorption. Table 1 provides the hydrogen uptake, TOF, and apparent activation energies for each catalyst. However, it should be noted that Fe in the presence of a more reducible metal, such as Ru, could result in Fe adsorbing H<sub>2</sub> under the chemisorption conditions [75]. Therefore, the values reported for RuFeK based catalysts are actually an underestimation of the total number of sites, since a stoichiometry of 1:1 H<sub>2</sub>:Ru was used to calculate TOF.

**Table 1.** H<sub>2</sub> uptake, turnover frequencies (TOF) and apparent activation energies (E<sub>a</sub>) for Sr and Fe substituted catalysts as compared to 4,12 RuK and unpromoted 4 Ru catalyst.

Catalyst	H <sub>2</sub> Uptake ( $\mu\text{mol H}_2/\text{g}$ )	TOF (s <sup>-1</sup> )			E <sub>a</sub> (kJ/mol)
		300 °C	350 °C	400 °C	
4 Ru	6.50	0.00	0.00	0.14	125.2 ± 8.9
4,12 RuK	4.70	0.13	0.26	0.33	65.7 ± 7.7
3,1,12 RuSrK	1.90	0.16	0.43	0.88	149.6 ± 4.1
2,2,12 RuSrK	0.90	0.38	0.81	1.38	153.7 ± 2.4
1,3,12 RuSrK	0.75	0.47	1.10	1.78	156.4 ± 1.6
3,1,12 RuFeK	0.76	0.00	0.35	0.97	248.1 ± 3.0
2,2,12 RuFeK	0.10	0.00	0.03	0.41	226.6 ± 2.9
1,3,12 RuFeK	1.20	0.00	0.00	0.28	250.9 ± 7.6

With the addition of K to the 4 Ru catalyst, the apparent activation energy decreases from 125.2 kJ/mol to 65.7 kJ/mol and resulted in the suppression of H<sub>2</sub> adsorption (at constant Ru wt%). Other apparent activations energies have been reported in a range from 87.9–155 kJ/mol [20,27,76,77] for supported Ru catalysts, which agrees with the results that are presented here. The decrease in apparent activation energy suggests electronic modification of the active sites, which has been thoroughly discussed in literature [34]. The Sr and Fe containing catalysts both exhibited a higher calculated apparent activation energy than the 4,12 RuK and 4 Ru catalyst, with the Sr catalysts within the range of 149.6–156.4 kJ/mol, and the Fe containing catalysts within the range of 226.6–250.9 kJ/mol. The apparent activation energy for the Fe containing catalysts is much higher than that calculated for the recombinative desorption of N<sub>2</sub> on Ru (001) crystal, which was found to be roughly 184 kJ/mol [78].

Microkinetic modeling determined that the dehydrogenation of adsorbed  $\text{NH}_3$  and adsorbed  $\text{NH}_2$  yielded an activation energy of 43.9 and 65.3 kJ/mol, respectively, while the dehydrogenation of adsorbed  $\text{NH}$  has a much higher activation energy of 161.5 kJ/mol [64]. Therefore, the addition of Sr seems to change the rate limiting step from the recombinative adsorption of  $\text{N}_2$  on 4 Ru, to some combination of dehydrogenation of  $\text{NH}$  species on the surface, based on the apparent activation energies calculated here. This seems to be independent of the Ru and Sr weight loadings, since we do not observe a strong change in apparent activation energy with changes in the amount of Ru and Sr. The change in the rate limiting step on different metal surfaces has been previously confirmed [63]. However, little work has been reported regarding the influence of promoters. In contrast, for the Fe based catalyst, the change in the apparent activation energy is almost double that of the baseline 4 Ru catalyst, indicating a dramatic change in the active sites of the catalyst when Fe is co-added.

The ammonia decomposition activity of these catalysts was evaluated in a single channel reactor to further probe the catalytic performance beyond the capabilities of the high throughput reactor. Each catalyst was tested under 100%  $\text{NH}_3$  and 5400 mL/hr/g<sub>cat</sub>. The catalytic performance for ammonia decomposition is shown in Figure 7a,b for Sr and Fe, respectively.

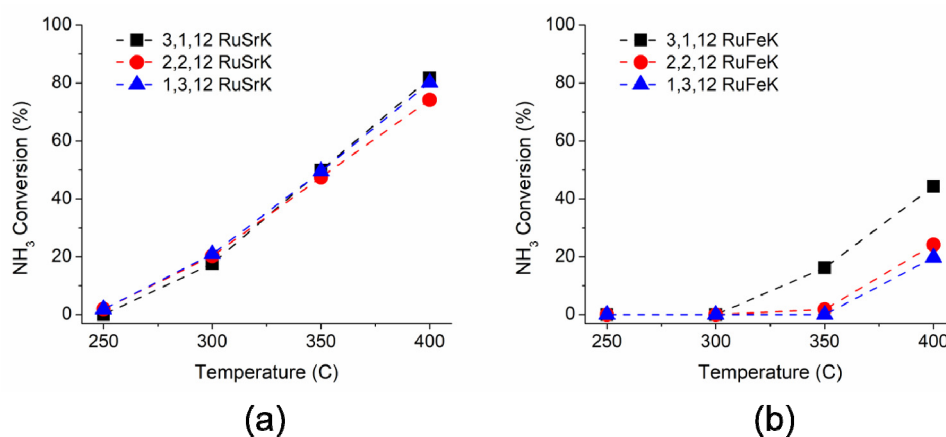


**Figure 7.** Ammonia decomposition activity of (a) 3,1,12 RuSrK, 2,2,12 RuSrK, and 1,3,12 RuSrK and of (b) 3,1,12 RuFeK, 2,2,12 RuFeK, and 1,3,12 RuFeK. Reaction conditions: 100%  $\text{NH}_3$ , 1.01 bar, and 5400 mL/hr/g<sub>cat</sub>.

Upon increasing the ammonia concentration from 1% in the initial screen to 100%, all of the catalysts showed a decline in the rate of reaction at 300 °C when compared to the activity from the initial screen, as shown in Figure 2 (and at all other subsequent temperatures, as shown in Figure S2–S4). Previous studies have observed a similar negative dependence on the ammonia partial pressure [64]. For the Sr based catalysts, each of the three weight loadings exhibited similar activity in the range of 250–400 °C with the 3,1,12 RuSrK catalyst obtaining 82% conversion at 400 °C. When the weight loading of Ru was lowered to 1,3,12 RuSrK, the activity declined to only 80%. However, the 1,3,12 RuSrK exhibited the highest TOF of all catalysts studied of 1.78 s<sup>-1</sup> at 400 °C, while the 3,1,12 RuSrK exhibited a TOF of 0.88 s<sup>-1</sup> at 400 °C.

The Fe based catalysts showed a larger distribution of activity across the three weight loadings and showed no activity at 300 °C in contrast to the Sr catalysts. Additionally, the 1,3,12 RuFeK catalysts have a TOF of 0.28 s<sup>-1</sup> at 400 °C, which was the lowest TOF of the promoted catalysts. The 3,1,12 RuFeK achieved 16% conversion at 350 °C and 74% conversion at 400 °C. In contrast, the 1,3,12 RuFeK achieved 42% conversion at 400 °C.

### 3.3.3. Effects of K, Fe and Sr on the Adsorption of CO on Ru

The adsorption of CO as a probe molecule on these catalysts was investigated through FT-IR spectroscopy to further understand the differences between the Sr and Fe based catalysts. The spectra of

room temperature CO adsorption for 1,3,12 RuSrK, 1,3,12 RuFeK are shown in Figure 8 in comparison to the 4 Ru and 4,12 RuK catalyst.

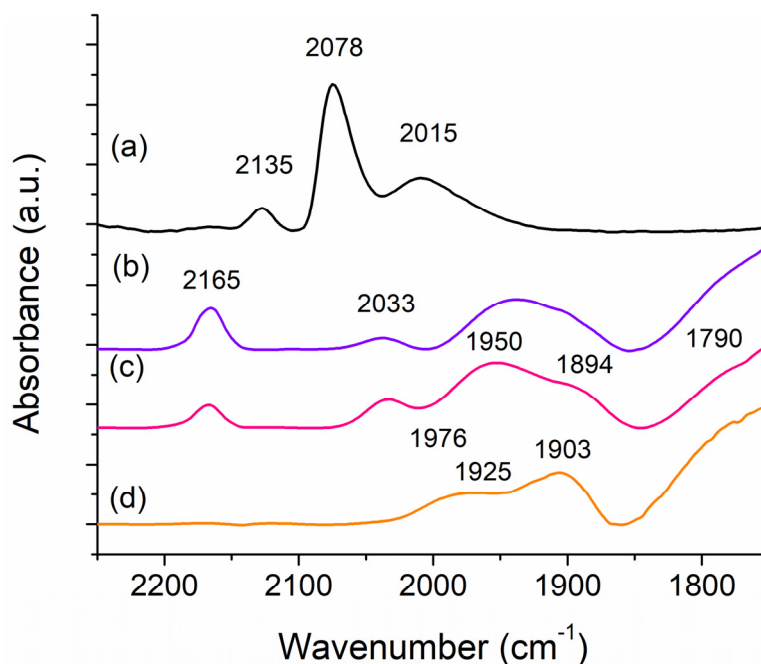


**Figure 8.** FT-IR spectra of CO adsorption on (a) 4 Ru (b) 4,12 RuK (c) 1,3,12 RuSrK and (d) 1,3,12 RuFeK.

The 4,12 RuK catalyst that is shown in Figure 8b exhibited four primary features: a strong band at  $2165\text{ cm}^{-1}$ , a weak band at  $2033\text{ cm}^{-1}$ , a broad feature between  $1995\text{ cm}^{-1}$  and  $1850\text{ cm}^{-1}$ , and a shoulder located at  $1790\text{ cm}^{-1}$ . The peak at  $2033\text{ cm}^{-1}$  is commonly attributed to linearly adsorbed CO on metallic Ru and its peak position has been shown to be a function of CO coverage [79–83], due to the dipole-dipole interactions between neighboring adsorbed CO molecules [84]. This peak is also present in the 1,3,12 RuSrK spectra (Figure 8c), but is absent in the 1,3,12 RuFeK (Figure 8d). In the 1,3,12 RuFeK spectrum, the peak maximum at  $1975\text{ cm}^{-1}$  may be attributed to the adsorption of CO on Fe [85]. Additionally, we see the suppression of any absorption bands in the  $2200$  to  $2000\text{ cm}^{-1}$  region. Fe might act to suppress the adsorption of CO on Ru, as this has been reported to occur with the addition of Fe to Rh/SiO<sub>2</sub> [86,87]. Interestingly, the relative intensity of the band at  $2033\text{ cm}^{-1}$  is relatively larger in the Sr spectrum in comparison to the 4,12 RuK, even with a lowered number of adsorption sites, thus suggesting that the addition of Sr changes the concentration of sites that will linearly adsorb CO, and that the addition of Fe causes their suppression.

Other studies of CO adsorption on Ru catalysts often report a weak band at about  $2135\text{ cm}^{-1}$  in conjunction with a stronger band at  $2078\text{ cm}^{-1}$ , which are attributed to the CO vibration of multicarbonyl surface species [79–81]. This band is evident for the 4 Ru catalyst, but it is absent upon the addition of K to the catalysts, which has been previously reported [83,84]. The 4 Ru catalyst additionally contains a broad band at  $2015\text{ cm}^{-1}$  that is suppressed with K addition, and it is related to the vibration of dicarbonyl species, as well as adsorbed CO on under-coordinated Ru, or high energy defect sites [81]. The suppression of these peaks with the addition of K has been hypothesized to be due to the blocking of under-coordinated Ru sites, which in turn suppresses hydrogen adsorption [84]. This is further evidenced by the reduction in H<sub>2</sub> uptake that was exhibited in the 4,12 RuK catalyst compared to the 4 Ru catalyst (Table 1).

Alkali addition to catalysts has also been known to show largely new interactions with CO in the low frequency range. This might be due to the interaction of CO with an electropositive center, which might weaken the CO bond and make it more reactive. Additives to metal catalysts have previously been shown to form new IR features due to the interaction between CO and the additive,



at frequencies lower than CO adsorbed on the unpromoted metal [84]. The range of adsorption and bonding configuration of CO on K pre-covered Ru(0001) surface, for example, has been shown through high resolution electron energy loss spectroscopy (HREELS) to be a function of both the CO and K coverage and that K addition can shift the CO stretch frequencies from  $2000\text{ cm}^{-1}$  to as low as  $1400\text{ cm}^{-1}$  [88–90]. Other studies of CO adsorption of K-Ru catalysts have reported bands at  $1995\text{ cm}^{-1}$ ,  $1950\text{ cm}^{-1}$ , and  $1940\text{ cm}^{-1}$  [83,84], as well as the broadening of peaks and more asymmetrical spectra with the addition of K [83]. K addition weakens the CO bond and strengthens the Ru-CO bond. Therefore, the band at  $2165\text{ cm}^{-1}$  in the 4,12 RuK and 1,3,12 RuSrK spectra might be due to the linearly adsorbed CO on partially oxidized  $\text{Ru}^{n+}$  ( $n = 1\text{--}3$ ) which has been previously reported as such [79,81]. Here, the Ru might become partially oxidized  $\text{Ru}^{n+}$  from the adsorption and subsequent dissociation of CO due to the weakening of the CO bond with the addition of K.

With the further addition of Sr and Fe, we see changes in the relative intensities of the absorption bands in the  $2000\text{ cm}^{-1}$  to  $1850\text{ cm}^{-1}$  region, as shown in Figure 8c,d, respectively. The addition of Sr results in two distinct peak maxima located at  $1950\text{ cm}^{-1}$  and  $1894\text{ cm}^{-1}$ , with respect to the 4,12 RuK catalyst. In contrast, the 1,3,12 RuFeK catalyst exhibits a shift to higher frequencies of this absorption region, with three peak maxima being located at  $1976\text{ cm}^{-1}$ ,  $1925\text{ cm}^{-1}$ , and  $1903\text{ cm}^{-1}$ . Additionally, the shoulder located at  $1790\text{ cm}^{-1}$  in 1,3,12 RuSrK and 4,12 RuK spectra can be attributed to bridge bonded CO [81,90]. This stretch is not observed for the 4 Ru catalyst (Figure 8a). This stretch has previously been reported to be broader and weaker than reported here [83,91], but these studies only use 3 wt% K, as well as different synthesis methods. Single crystal studies have shown a dramatic increase in bridge bonded CO on Pt(111) and Rh(111) as alkali coverage on these metals increases [92,93]. Therefore, the electropositive nature of Sr might act to similarly weaken the CO bond through further charge transfer, thus resulting in a more prominent low frequency band centered at  $1880\text{ cm}^{-1}$ , which results in a weakened CO bond, as well an increase in the amount bridge bonded CO with such low Ru content, as compared to 4,12 RuK catalyst.

#### 4. Conclusions

We demonstrated the utilization of high throughput screening to determine low cost substitutional materials for low temperature ammonia decomposition. This screen concluded that substitution of Ru with Mg, Ca, Sr, Sc, Y, Ta, Hf, and Zr resulted in catalyst formulations that were more active than a baseline 4,12 RuK catalyst with less Ru content. Additionally, we were able to determine that, with the addition of Y, Hf, Zr, and Sr, the Ru content could be lowered by a factor of four, without an apparent loss in activity. XRD analysis confirmed that these catalysts contained Ru mixed metal oxides of the form  $\text{KRu}_4\text{O}_8$  and  $\text{KRuO}_4$ . These structures enable close contact between the K promoter and the Ru active sites, thus enhancing electron donation from K to Ru and modifying the reactivity of the catalysts.

Further investigation into the Sr and Fe based catalysts confirmed that the addition of Sr did not act to change the apparent activation energy of the catalyst with each of the three weight loadings studied. Additionally, FT-IR analysis of CO adsorption revealed that the addition of Sr resulted in weakened CO bonds on Ru sites due to its electropositive nature, being accompanied by strongly adsorbed linear CO. The addition of other electropositive elements, such as K, Li, and Na, has shown a positive effect on ammonia decomposition, and to further facilitate the RDS [94]. This might be analogous to the weakening of N-H bonds of adsorbed ammonia and thus facilitating the dehydrogenation of ammonia. A catalyst containing 1,3,12 RuSrK was shown to achieve a TOF of  $1.78\text{ s}^{-1}$  at  $40\text{ }^\circ\text{C}$ , which is five times the TOF of 4,12 RuK at the same temperature. These materials were discovered through the systematic utilization of high throughput screening, which successfully resulted in catalysts that were highly active in 100%  $\text{NH}_3$ , which shows their potential for on-site  $\text{H}_2$  generation technologies.



## 5. Patents

Lauterbach J., McCullough K., “Ammonia Decomposition Catalyst Systems,” US Patent App.: 16/376,158; 2020.

**Supplementary Materials:** The following are available online at <http://www.mdpi.com/1996-1944/13/8/1869/s1>, Figure S1. Thermodynamic limit of ammonia decomposition at 101.325 kPa, Figure S2. Catalytic activity at 250 °C, Figure S3. Catalytic activity at 350 °C, Figure S4. Catalytic activity at 400 °C, Figure S5. Arrhenius plot for 4 Ru and 4,12 RuK, Table S1. Summary of the Ru species present in each catalyst, Figure S6. XRD patterns of (from bottom to top): 1,3,12 RuCuK, 2,2,12 RuCuK and 3,1,12 RuCuK, Figure S7. XRD patterns of (from bottom to top): 1,3,12 RuYK, 2,2,12 RuYK and 3,1,12 RuYK, Figure S8. XRD patterns of (from bottom to top): 1,3,12 RuAuK, 2,2,12 RuAuK and 3,1,12 RuAuK, Figure S9. XRD patterns of (from bottom to top): 1,3,12 RuNiK, 2,2,12 RuNiK and 3,1,12 RuNiK, Figure S10. XRD patterns of (from bottom to top): 1,3,12 RuInK, 2,2,12 RuInK and 3,1,12 RuInK, Figure S11. XRD patterns of (from bottom to top): 1,3,12 RuNbK, 2,2,12 RuNbK and 3,1,12 RuNbK, Figure S12. XRD patterns of (from bottom to top): 1,3,12 RuMnK, 2,2,12 RuMnK and 3,1,12 RuMnK, Figure S13. XRD patterns of (from bottom to top): 1,3,12 RuAgK, 2,2,12 RuAgK and 3,1,12 RuAgK, Figure S14. XRD patterns of (from bottom to top): 1,3,12 RuPtK, 2,2,12 RuPtK and 3,1,12 RuPtK, Figure S15. XRD patterns of (from bottom to top): 1,3,12 RuZrK, 2,2,12 RuZrK and 3,1,12 RuZrK, Figure S16. XRD patterns of (from bottom to top): 1,3,12 RuReK, 2,2,12 RuReK and 3,1,12 RuReK, Figure S17. XRD patterns of (from bottom to top): 1,3,12 RuIrK, 2,2,12 RuIrK and 3,1,12 RuIrK, Figure S18. XRD patterns of (from bottom to top): 1,3,12 RuCoK, 2,2,12 RuCoK and 3,1,12 RuCoK, Figure S19. XRD patterns of (from bottom to top): 1,3,12 RuWK, 2,2,12 RuWK and 3,1,12 RuWK, Figure S20. XRD patterns of (from bottom to top): 1,3,12 RuCaK, 2,2,12 RuCaK and 3,1,12 RuCaK, Figure S21. XRD patterns of (from bottom to top): 1,3,12 RuHfK, 2,2,12 RuHfK and 3,1,12 RuHfK, Figure S22. XRD patterns of (from bottom to top): 1,3,12 RuSnK, 2,2,12 RuSnK and 3,1,12 RuSnK, Figure S23. XRD patterns of (from bottom to top): 1,3,12 RuZnK, 2,2,12 RuZnK and 3,1,12 RuZnK, Figure S24. XRD patterns of (from bottom to top): 1,3,12 RuOsK, 2,2,12 RuOsK and 3,1,12 RuOsK, Figure S25. XRD patterns of (from bottom to top): 1,3,12 RuPbK, 2,2,12 RuPbK and 3,1,12 RuPbK, Figure S26. XRD patterns of (from bottom to top): 1,3,12 RuMoK, 2,2,12 RuMoK and 3,1,12 RuMoK, Figure S27. XRD patterns of (from bottom to top): 1,3,12 RuCrK, 2,2,12 RuCrK and 3,1,12 RuCrK, Figure S28. XRD patterns of (from bottom to top): 1,3,12 RuScK, 2,2,12 RuScK and 3,1,12 RuScK, Figure S29. XRD patterns of (from bottom to top): 1,3,12 RuPdK, 2,2,12 RuPdK and 3,1,12 RuPdK, Figure S30. XRD patterns of (from bottom to top): 1,3,12 RuMgK, 2,2,12 RuMgK and 3,1,12 RuMgK, Figure S31. XRD patterns of (from bottom to top): 1,3,12 RuBiK, 2,2,12 RuBiK and 3,1,12 RuBiK, Figure S32. XRD patterns of (from bottom to top): 1,3,12 RuCdK, 2,2,12 RuCdK and 3,1,12 RuCdK.

**Author Contributions:** Conceptualization of project, K.M. and J.A.L.; methodology, characterization and synthesis, K.M. and P.-H.C.; formal analysis of high throughput data, FTIR spectra and XRD patterns, K.M.; investigation of activation energies and turnover frequencies, K.M.; writing—original draft preparation, K.M.; writing—review and editing, K.M., J.D.J. and J.A.L. All authors have read and agreed to the published version of the manuscript.

**Funding:** Financial support from the South Carolina Center of Economic Excellence for Strategic Approaches to the Generation of Electricity is highly appreciated as well as support from the US National Science Foundation, grants DGE 1250052 and the Department of Energy, ARPA-E Contract No. DE-AR0000931.

**Conflicts of Interest:** The authors declare no conflict of interest

## References

1. Mukherjee, S.; Devaguptapu, S.V.; Sviripa, A.C.; Lund, R.F.; Wu, G. Low-temperature ammonia decomposition catalysts for hydrogen generation. *Appl. Catal. B Environ.* **2018**, *226*, 162–181. [\[CrossRef\]](#)
2. Christensen, C.H.; Johannessen, T.; Sørensen, R.Z.; Nørskov, J.K. Towards an ammonia-mediated hydrogen economy? *Catal. Today* **2006**, *111*, 140–144. [\[CrossRef\]](#)
3. Bell, T.E. H<sub>2</sub> Production via Ammonia Decomposition Using Non-Noble Metal Catalysts: A Review. *Top. Catal.* **2016**, *59*, 1438–1457. [\[CrossRef\]](#)
4. Sørensen, R.Z.; Nielsen, L.J.E.; Jensen, S.; Hansen, O.; Johannessen, T.; Quaade, U.; Christensen, C.H. Catalytic ammonia decomposition: Miniaturized production of CO<sub>x</sub>-free hydrogen for fuel cells. *Catal. Commun.* **2005**, *6*, 229–232. [\[CrossRef\]](#)
5. Zhang, J.; Comotti, M.; Schüth, F.; Schlögl, R.; Su, D.S. Commercial Fe- or Co-containing carbon nanotubes as catalysts for NH<sub>3</sub> decomposition. *Chem. Commun.* **2007**, *19*, 1916–1918. [\[CrossRef\]](#)
6. Lu, A.-H.H.; Nitz, J.-J.J.; Comotti, M.; Weidenthaler, C.; Schlichte, K.; Lehmann, C.W.; Terasaki, O.; Schüth, F. Spatially and Size Selective Synthesis of Fe-Based Nanoparticles on Ordered Mesoporous Supports as Highly Active and Stable Catalysts for Ammonia Decomposition. *J. Am. Chem. Soc.* **2010**, *132*, 14152–14162. [\[CrossRef\]](#)

7. Ji, J.; Duan, X.; Qian, G.; Li, P.; Zhou, X.; Chen, D.; Yuan, W. Fe particles on the tops of carbon nanofibers immobilized on structured carbon microfibers for ammonia decomposition. *Catal. Today* **2013**, *216*, 254–260. [[CrossRef](#)]
8. Duan, X.; Qian, G.; Zhou, X.; Sui, Z.; Chen, D.; Yuan, W. Tuning the size and shape of Fe nanoparticles on carbon nanofibers for catalytic ammonia decomposition. *Appl. Catal. B Environ.* **2011**, *101*, 189–196. [[CrossRef](#)]
9. Li, L.; Jiang, R.; Chu, W.; Cang, H.; Chen, H.; Yan, J. Cobalt nanoparticles embedded in a porous carbon matrix as an efficient catalyst for ammonia decomposition. *Catal. Sci. Technol.* **2017**, *7*, 1363–1371. [[CrossRef](#)]
10. Podila, S.; Driss, H.; Zaman, S.F.; Alhamed, Y.A.; Alzahrani, A.A.; Daous, M.A.; Petrov, L.A. Hydrogen generation by ammonia decomposition using Co/MgO-La<sub>2</sub>O<sub>3</sub> catalyst: Influence of support calcination atmosphere. *J. Mol. Catal. A Chem.* **2016**, *414*, 130–139. [[CrossRef](#)]
11. Varisli, D.; Kaykac, N.G. Hydrogen from ammonia over cobalt incorporated silicate structured catalysts prepared using different cobalt salts. *Int. J. Hydrogen Energy* **2016**, *41*, 5955–5968. [[CrossRef](#)]
12. Yin, S.-F.; Zhang, Q.-H.; Xu, B.-Q.; Zhu, W.-X.; Ng, C.-F.; Au, C.-T. Investigation on the catalysis of CO<sub>x</sub>-free hydrogen generation from ammonia. *J. Catal.* **2004**, *224*, 384–396. [[CrossRef](#)]
13. Li, X.K.; Ji, W.J.; Zhao, J.; Wang, S.J.; Au, C.T. Ammonia decomposition over Ru and Ni catalysts supported on fumed SiO<sub>2</sub>, MCM-41, and SBA-15. *J. Catal.* **2005**, *236*, 181–189. [[CrossRef](#)]
14. Liu, H.; Wang, H.; Shen, J.; Sun, Y.; Liu, Z. Preparation, characterization and activities of the nano-sized Ni/SBA-15 catalyst for producing CO<sub>x</sub>-free hydrogen from ammonia. *Appl. Catal. A Gen.* **2008**, *337*, 138–147. [[CrossRef](#)]
15. Li, Y.; Wen, J.; Ali, A.M.; Duan, M.; Zhu, W.; Zhang, H.; Chen, C.; Li, Y. Size structure-catalytic performance correlation of supported Ni/MCF-17 catalysts for CO<sub>x</sub>-free hydrogen production. *Chem. Commun.* **2018**, *54*, 6364–6367. [[CrossRef](#)] [[PubMed](#)]
16. Zheng, W.; Zhang, J.; Ge, Q.; Xu, H.; Li, W. Effects of CeO<sub>2</sub> addition on Ni/Al<sub>2</sub>O<sub>3</sub> catalysts for the reaction of ammonia decomposition to hydrogen. *Appl. Catal. B Environ.* **2008**, *80*, 98–105. [[CrossRef](#)]
17. Inokawa, H.; Ichikawa, T.; Miyaoka, H. Catalysis of nickel nanoparticles with high thermal stability for ammonia decomposition. *Appl. Catal. A Gen.* **2015**, *491*, 184–188. [[CrossRef](#)]
18. Li, L.; Zhu, Z.H.; Wang, S.B.; Yao, X.D.; Yan, Z.F. Chromium oxide catalysts for CO<sub>x</sub>-free hydrogen generation via catalytic ammonia decomposition. *J. Mol. Catal. A Chem.* **2009**, *304*, 71–76. [[CrossRef](#)]
19. Hajduk, Š.; Dasireddy, V.D.B.C.; Likožar, B.; Dražič, G.; Orel, Z.C. CO<sub>x</sub>-free hydrogen production via decomposition of ammonia over Cu–Zn-based heterogeneous catalysts and their activity/stability. *Appl. Catal. B Environ.* **2017**, *211*, 57–67. [[CrossRef](#)]
20. Bradford, M.C.J.J.; Fanning, P.E.; Vannice, M.A. Kinetics of NH<sub>3</sub> Decomposition over Well Dispersed Ru. *J. Catal.* **1997**, *172*, 479–484. [[CrossRef](#)]
21. Egawa, C.; Nishida, T.; Naito, S.; Tamaru, K. Ammonia decomposition on (1 1 10) and (0 0 1) surfaces of ruthenium. *J. Chem. Soc. Faraday Trans. Phys. Chem. Condens. Phases* **1984**, *80*, 1595–1604. [[CrossRef](#)]
22. Dahl, S.; Törnqvist, E.; Chorkendorff, I. Dissociative adsorption of N<sub>2</sub> on Ru(0001): A surface reaction totally dominated by steps. *J. Catal.* **2000**, *192*, 381–390. [[CrossRef](#)]
23. Boisen, A.; Dahl, S.; Nørskov, J.K.; Christensen, C.H. Why the optimal ammonia synthesis catalyst is not the optimal ammonia decomposition catalyst. *J. Catal.* **2005**, *230*, 309–312. [[CrossRef](#)]
24. Raróg, W.; Kowalczyk, Z.; Sentek, J.; Składanowski, D.; Zieliński, J. Effect of K, Cs and Ba on the kinetics of NH<sub>3</sub> synthesis over carbon-based ruthenium catalysts. *Catal. Lett.* **2000**, *68*, 163–168. [[CrossRef](#)]
25. Raróg-Pilecka, W.; Szmigiel, D.; Kowalczyk, Z.; Jodzis, S.; Zielinski, J. Ammonia decomposition over the carbon-based ruthenium catalyst promoted with barium or cesium. *J. Catal.* **2003**, *218*, 465–469. [[CrossRef](#)]
26. Raróg-Pilecka, W.; Miśkiewicz, E.; Szmigiel, D.; Kowalczyk, Z. Structure sensitivity of ammonia synthesis over promoted ruthenium catalysts supported on graphitised carbon. *J. Catal.* **2005**, *231*, 11–19. [[CrossRef](#)]
27. Hill, A.K.; Torrente-Murciano, L. In-situ H<sub>2</sub> production via low temperature decomposition of ammonia: Insights into the role of cesium as a promoter. *Int. J. Hydrogen Energy* **2014**, *39*, 7646–7654. [[CrossRef](#)]
28. Yu, P.; Guo, J.; Liu, L.; Wang, P.; Chang, F.; Wang, H.; Ju, X.; Chen, P. Effects of Alkaline Earth Metal Amides on Ru in Catalytic Ammonia Decomposition. *J. Phys. Chem. C* **2016**, *120*, 2822–2828. [[CrossRef](#)]

29. Kishida, K.; Kitano, M.; Inoue, Y.; Sasase, M.; Nakao, T.; Tada, T.; Abe, H.; Niwa, Y.; Yokoyama, T.; Hara, M.; et al. Large Oblate Hemispheroidal Ruthenium Particles Supported on Calcium Amide as Efficient Catalysts for Ammonia Decomposition. *Chem. A Eur. J.* **2018**, *24*, 7976–7984. [[CrossRef](#)]
30. Karim, A.M.; Prasad, V.; Mpourmpakis, G.; Lonergan, W.W.; Frenkel, A.I.; Chen, J.G.; Vlachos, D.G. Correlating particle size and shape of supported Ru/ $\gamma$ -Al<sub>2</sub>O<sub>3</sub> catalysts with NH<sub>3</sub> decomposition activity. *J. Am. Chem. Soc.* **2009**, *131*, 12230–12239. [[CrossRef](#)]
31. Jacobsen, C.J.H.; Dahl, S.; Hansen, P.L.; Törnqvist, E.; Jensen, L.; Topsøe, H.; Prip, D.V.; Møenshaug, P.B.; Chorkendorff, I. Structure sensitivity of supported ruthenium catalysts for ammonia synthesis. *J. Mol. Catal. A Chem.* **2000**, *163*, 19–26. [[CrossRef](#)]
32. Szmigiel, D.; Bielawa, H.; Kurtz, M.; Hinrichsen, O.; Muhler, M.; Ra, W.; Jodzis, S.A.; Kowalczyk, Z.; Znak, L.; Zielí, J. The Kinetics of Ammonia Synthesis over Ruthenium-Based Catalysts: The Role of Barium and Cesium. *J. Catal.* **2002**, *205*, 205–212. [[CrossRef](#)]
33. Ju, X.; Liu, L.; Zhang, X.; Feng, J.; He, T.; Chen, P. Highly Efficient Ru/MgO Catalyst with Surface-Enriched Basic Sites for Production of Hydrogen from Ammonia Decomposition. *ChemCatChem* **2019**, *11*, 4161–4170. [[CrossRef](#)]
34. Yin, S.F.; Xu, B.Q.; Zhu, W.X.; Ng, C.F.; Zhou, X.P.; Au, C.T. Carbon nanotubes-supported Ru catalyst for the generation of CO<sub>x</sub>-free hydrogen from ammonia. *Catal. Today* **2004**, *93–95*, 27–38. [[CrossRef](#)]
35. Ju, X.; Liu, L.; Yu, P.; Guo, J.; Zhang, X.; He, T.; Wu, G.; Chen, P. Mesoporous Ru/MgO prepared by a deposition-precipitation method as highly active catalyst for producing CO<sub>x</sub>-free hydrogen from ammonia decomposition. *Appl. Catal. B Environ.* **2017**, *211*, 167–175. [[CrossRef](#)]
36. Hu, Z.; Mahin, J.; Datta, S.; Bell, T.E.; Torrente-Murciano, L. Ru-Based Catalysts for H<sub>2</sub> Production from Ammonia: Effect of 1D Support. *Top. Catal.* **2018**, *1*, 1–3. [[CrossRef](#)]
37. Jacobsen, C.J.H.; Dahl, S.; Clausen, B.G.S.; Bahn, S.; Logadottir, A.; Nørskov, J.K. Catalyst design by interpolation in the periodic table: Bimetallic ammonia synthesis catalysts. *J. Am. Chem. Soc.* **2001**, *123*, 8404–8405. [[CrossRef](#)]
38. Duan, X.; Qian, G.; Zhou, X.; Chen, D.; Yuan, W. MCM-41 supported CoMo bimetallic catalysts for enhanced hydrogen production by ammonia decomposition. *Chem. Eng. J.* **2012**, *207–208*, 103–108. [[CrossRef](#)]
39. Ji, J.; Duan, X.; Qian, G.; Zhou, X.; Tong, G.; Yuan, W. Towards an efficient CoMo/ $\gamma$ -Al<sub>2</sub>O<sub>3</sub> catalyst using metal amine metallate as an active phase precursor: Enhanced hydrogen production by ammonia decomposition. *Int. J. Hydrogen Energy* **2014**, *39*, 12490–12498. [[CrossRef](#)]
40. Zhang, J.; Müller, J.O.; Zheng, W.; Wang, D.; Su, D.; Schlögl, R. Individual Fe-Co alloy nanoparticles on carbon nanotubes: Structural and catalytic properties. *Nano Lett.* **2008**, *8*, 2738–2743. [[CrossRef](#)]
41. Simonsen, S.B.; Chakraborty, D.; Chorkendorff, I.; Dahl, S. Alloyed Ni-Fe nanoparticles as catalysts for NH<sub>3</sub> decomposition. *Appl. Catal. A Gen.* **2012**, *447–448*, 22–31. [[CrossRef](#)]
42. Sasmaz, E.; Mingle, K.; Lauterbach, J. High-throughput screening using Fourier-transform infrared imaging. *Engineering* **2015**, *1*, 234–242. [[CrossRef](#)]
43. Hendershot, J.; Reed, J.; Lasko, S.S.; Fellmann, M.-F.; Oskarsdottir, G.; Delgass, W.; Snively, C.M. A novel reactor system for high throughput catalyst testing under realistic conditions. *Appl. Catal. A* **2003**, *254*, 107–120. [[CrossRef](#)]
44. Betancourt, P.; Rives, A.; Hubaut, R.; Scott, C.E.; Goldwasser, J. A study of the ruthenium-alumina system. *Appl. Catal. A Gen.* **1998**, *170*, 307–314. [[CrossRef](#)]
45. Pyrz, W.; Vijay, R.; Binz, J.; Lauterbach, J.; Buttrey, D.J. Characterization of K-promoted Ru catalysts for ammonia decomposition discovered using high-throughput experimentation. *Top. Catal.* **2008**, *50*, 180–191. [[CrossRef](#)]
46. Yin, S.F.; Xu, B.Q.; Zhou, X.P.; Au, C.T. A mini-review on ammonia decomposition catalysts for on-site generation of hydrogen for fuel cell applications. *Appl. Catal. A Gen.* **2004**, *277*, 1–9. [[CrossRef](#)]
47. Czekajło, Ł.; Lendzion-Bieluń, Z. Effect of preparation conditions and promoters on the structure and activity of the ammonia decomposition reaction catalyst based on nanocrystalline cobalt. *Chem. Eng. J.* **2016**, *289*, 254–260. [[CrossRef](#)]

48. Foo, M.L.; Lee, W.-L.; Siegrist, T.; Lawes, G.; Ramirez, A.P.; Ong, N.P.; Cava, R.J. Electronic characterization of alkali ruthenium hollandites:  $\text{KRu}_4\text{O}_8$ ,  $\text{RbRu}_4\text{O}_8$  and  $\text{Cs}_{0.8}\text{Li}_{0.2}\text{Ru}_4\text{O}_8$ . *Mater. Res. Bull.* **2004**, *39*, 1663–1670. [[CrossRef](#)]
49. Wang, C.; Sun, L.; Cao, Q.; Hu, B.; Huang, Z.; Tang, X. Surface structure sensitivity of manganese oxides for low-temperature selective catalytic reduction of NO with  $\text{NH}_3$ . *Appl. Catal. B Environ.* **2010**, *101*, 598–605. [[CrossRef](#)]
50. Laurita, G.; Grajczyk, R.; Stolt, M.; Coutinho, I.; Sleight, A.W.; Subramanian, M.A. Influence of Structural Disorder on Hollandites  $\text{AxRu}_4\text{O}_8$  ( $\text{A} = \text{K, Rb, Rb}_{1-x}\text{Na}_x$ ). *Inorg. Chem.* **2016**, *55*, 3462–3467. [[CrossRef](#)]
51. Lin, B.; Wang, R.; Yu, X.; Lin, J.; Xie, F.; Wei, K. Physicochemical characterization and  $\text{H}_2$ -TPD study of alumina supported ruthenium catalysts. *Catal. Lett.* **2008**, *124*, 178–184. [[CrossRef](#)]
52. Yunrui, Z.; Wanpeng, Z.; Fudong, L.; Jianbing, W.; Shaoxia, Y. Catalytic activity of  $\text{Ru}/\text{Al}_2\text{O}_3$  for ozonation of dimethyl phthalate in aqueous solution. *Chemosphere* **2007**, *66*, 145–150. [[CrossRef](#)] [[PubMed](#)]
53. Sellers, M.C.K.; Zussblatt, N.P.; Marsh, C.P. Potassium perruthenate-treated carbon nanotube sheets for flexible supercapacitors. *Electrochem. Commun.* **2012**, *18*, 58–61. [[CrossRef](#)]
54. Yang, H.M. *Characterization of Ammonia Decomposition Catalysts for Hydrogen Generation*; University of Delaware: Newark, DE, USA, 2008.
55. Dahl, S.; Logadottir, A.; Egeberg, R.; Nielsen, J.H.; Chorkendorff, I.; Tornqvist, E.; Norskov, J.K. Role of steps in N<sub>2</sub> activation on Ru(0001). *Phys. Rev. Lett.* **1999**, *83*, 1814–1817. [[CrossRef](#)]
56. Zhang, J.; Xu, H.; Li, W. Kinetic study of  $\text{NH}_3$  decomposition over Ni nanoparticles: The role of La promoter, structure sensitivity and compensation effect. *Appl. Catal. A Gen.* **2005**, *296*, 257–267. [[CrossRef](#)]
57. Williams, T.; McCullough, K.; Lauterbach, J.A. Enabling Catalyst Discovery through Machine Learning and High-Throughput Experimentation. *Chem. Mater.* **2020**, *32*, 157–165. [[CrossRef](#)]
58. Nagaoka, K.; Eboshi, T.; Abe, N.; Miyahara, S.; Honda, K.; Sato, K. Influence of basic dopants on the activity of  $\text{Ru}/\text{Pr}_6\text{O}_{11}$  for hydrogen production by ammonia decomposition. *Int. J. Hydrogen Energy* **2014**, *39*, 20731–20735. [[CrossRef](#)]
59. Liu, Y.; Ji, J.; Qian, G.; Yuan, W.; Duan, X.; Zhou, X.; Chen, D. Structure sensitivity of ammonia decomposition over Ni catalysts: A computational and experimental study. *Fuel Process. Technol.* **2012**, *108*, 112–117.
60. Zhou, S.; Lin, S.; Guo, H. First-Principles Insights into Ammonia Decomposition Catalyzed by Ru Clusters Anchored on Carbon Nanotubes: Size Dependence and Interfacial Effects. *J. Phys. Chem. C* **2018**, *122*, 9091–9100. [[CrossRef](#)]
61. Heracleous, E.; Lemonidou, A.A. Ni-Nb-O mixed oxides as highly active and selective catalysts for ethene production via ethane oxidative dehydrogenation. Part I: Characterization and catalytic performance. *J. Catal.* **2006**, *237*, 162–174. [[CrossRef](#)]
62. Hansen, T.W.; Wagner, J.B.; Hansen, P.L.; Dahl, S.; Topsøe, H.; Jacobsen, C.J.H. Atomic-resolution in situ transmission electron microscopy of a promoter of a heterogeneous catalyst. *Science* **2001**, *294*, 1508–1510. [[CrossRef](#)] [[PubMed](#)]
63. Ganley, J.C.; Thomas, F.S.; Seebauer, E.G.; Masel, R.I. A priori catalytic activity correlations: The difficult case of hydrogen production from ammonia. *Catal. Lett.* **2004**, *96*, 117–122. [[CrossRef](#)]
64. Prasad, V.; Karim, A.M.; Arya, A.; Vlachos, D.G. Assessment of overall rate expressions and multiscale, microkinetic model uniqueness via experimental data injection: Ammonia decomposition on  $\text{Ru}/\gamma\text{-Al}_2\text{O}_3$  for hydrogen production. *Ind. Eng. Chem. Res.* **2009**, *48*, 5255–5265. [[CrossRef](#)]
65. Al-Saleh, M.A.; Hossain, M.M.; Shalabi, M.A.; Kimura, T.; Inui, T. Hydrogen spillover effects on Pt-Rh modified Co-clay catalysts for heavy oil upgrading. *Appl. Catal. A Gen.* **2003**, *253*, 453–459. [[CrossRef](#)]
66. Lin, P.Y.; Meng, M.; Yuan, J.J.; Yu, S.M.; Fu, Y.L. Spillover effect and CO oxidation activity on the supported noble metals-metal oxides catalysts. *Stud. Surf. Sci. Catal.* **1997**, *112*, 201–210.
67. Wang, L.; Yin, C.; Yang, R.T. Selective catalytic reduction of nitric oxide with hydrogen on supported Pd: Enhancement by hydrogen spillover. *Appl. Catal. A Gen.* **2016**, *514*, 35–42. [[CrossRef](#)]
68. Nabaho, D.; Niemantsverdriet, J.W.; Claeys, M.; van Steen, E. Hydrogen spillover in the Fischer-Tropsch synthesis: An analysis of platinum as a promoter for cobalt-alumina catalysts. *Catal. Today* **2016**, *261*, 17–27. [[CrossRef](#)]



69. Hill, A.K.; Torrente-Murciano, L. Low temperature H<sub>2</sub> production from ammonia using ruthenium-based catalysts: Synergetic effect of promoter and support. *Appl. Catal. B Environ.* **2015**, *172–173*, 129–135. [[CrossRef](#)]
70. Falicov, L.M.; And, T.; Somorjai, G.A. Correlation between catalytic activity and bonding and coordination number of atoms and molecules on transition metal surfaces: Theory and experimental evidence. *Chemistry* **1985**, *82*, 2207–2211. [[CrossRef](#)]
71. Hammer, B.; Nørskov, J.K. Theoretical surface science and catalysis—calculations and concepts. *Impact Surf. Sci. Catal.* **2000**, *45*, 71–129.
72. Wang, Y.; Zhu, J.H.; Huang, W.Y. Synthesis and characterization of potassium-modified alumina superbases. *Phys. Chem. Chem. Phys.* **2001**, *3*, 2537–2543. [[CrossRef](#)]
73. Weisz, P.B.; Prater, C.D. Interpretation of Measurements in Experimental Catalysis. *Adv. Catal.* **1954**, *6*, 143–196.
74. Reid, R. Chapter 11: Diffusion Coefficients. In *The Properties of Gases and Liquids*; McGraw-Hill: New York, NY, USA, 1987.
75. Bartholomew, C.H. Hydrogen adsorption on supported cobalt, iron, and nickel. *Catal. Lett.* **1990**, *7*, 27–51. [[CrossRef](#)]
76. Choudhary, T.V.; Sivadinarayana, C.; Goodman, D.W. Catalytic ammonia decomposition: CO<sub>x</sub>-free hydrogen production for fuel cell applications. *Catal. Lett.* **2001**, *72*, 197–201. [[CrossRef](#)]
77. Di Carlo, A.; Vecchione, L.; del Prete, Z. Ammonia decomposition over commercial Ru/Al<sub>2</sub>O<sub>3</sub> catalyst: An experimental evaluation at different operative pressures and temperatures. *Int. J. Hydrogen Energy* **2014**, *39*, 808–814. [[CrossRef](#)]
78. Tsai, W.; Weinberg, W.H. Steady-state decomposition of ammonia on the Ru(001) surface. *J. Phys. Chem.* **1987**, *91*, 5302–5307. [[CrossRef](#)]
79. Panagiotopoulou, P. Methanation of CO<sub>2</sub> over alkali-promoted Ru/TiO<sub>2</sub> catalysts: II. Effect of alkali additives on the reaction pathway. *Appl. Catal. B Environ.* **2018**, *236*, 162–170. [[CrossRef](#)]
80. Abdel-Mageed, A.M.; Widmann, D.; Olesen, S.E.; Chorkendorff, I.; Biskupek, J.; Behm, R.J. Selective CO Methanation on Ru/TiO<sub>2</sub> Catalysts: Role and Influence of Metal-Support Interactions. *ACS Catal.* **2015**, *5*, 6753–6763. [[CrossRef](#)]
81. Chin, S.Y.; Williams, C.T.; Amiridis, M.D. FTIR studies of CO adsorption on Al<sub>2</sub>O<sub>3</sub>- and SiO<sub>2</sub>-supported Ru catalysts. *J. Phys. Chem. B* **2006**, *110*, 871–882. [[CrossRef](#)]
82. Solymosi, F.; Raskó, J. An infrared study of the influence of CO adsorption on the topology of supported ruthenium. *J. Catal.* **1989**, *115*, 107–119. [[CrossRef](#)]
83. Cao, S.; Monnier, J.R.; Regalbuto, J.R. Alkali promotion of alumina-supported ruthenium catalysts for hydrogenation of levulinic acid to  $\gamma$ -valerolactone. *J. Catal.* **2017**, *347*, 72–78. [[CrossRef](#)]
84. Waghay, A.; Wang, J.; Oukaci, R.; Blackmond, D.G. Influence of alkali promoters in the selective hydrogenation of 3-methyl-2-butenal over Ru/SiO<sub>2</sub> catalysts. *J. Phys. Chem.* **1992**, *96*, 5954–5959. [[CrossRef](#)]
85. Bradshaw, A.M.; Pritchard, J. Infrared spectra of carbon monoxide chemisorbed on metal films. A comparative study of copper, silver, gold, iron, cobalt and nickel. *Proc. R. Soc. Lond. Ser. A Math. Phys. Sci.* **1970**, *316*, 169–183.
86. Mo, X.; Gao, J.; Umnajkaseam, N.; Goodwin, J.G. La, V, and Fe promotion of Rh/SiO<sub>2</sub> for CO hydrogenation: Effect on adsorption and reaction. *J. Catal.* **2009**, *267*, 167–176. [[CrossRef](#)]
87. Ichikawa, M.; Fukushima, T. Infrared studies of metal additive effects on CO chemisorption modes on SiO<sub>2</sub>-supported Rh-Mn, -Ti, and -Fe catalysts. *J. Phys. Chem.* **1985**, *89*, 1564–1567. [[CrossRef](#)]
88. DePaola, R.A.; Hrbek, J.; Hoffmann, F.M. Potassium promoted C-O bond weakening on Ru(001). I. Through-metal interaction at low potassium precoverage. *J. Chem. Phys.* **1985**, *82*, 2484–2498. [[CrossRef](#)]
89. Politano, A.; Chiarello, G.; Benedek, G.; Chulkov, E.V.; Echenique, P.M. Vibrational spectroscopy and theory of alkali metal adsorption and co-adsorption on single-crystal surfaces. *Surf. Sci. Rep.* **2013**, *68*, 305–389. [[CrossRef](#)]
90. Hoffmann, F.M.; de Paola, R.A. Anomalous C-O bond weakening of side-on-bonded carbon monoxide on a potassium-promoted Ru(001) surface. *Phys. Rev. Lett.* **1984**, *52*, 1697–1700. [[CrossRef](#)]
91. Cao, S.; Monnier, J.R.; Williams, C.T.; Diao, W.; Regalbuto, J.R. Rational nanoparticle synthesis to determine the effects of size, support, and K dopant on Ru activity for levulinic acid hydrogenation to  $\gamma$ -valerolactone. *J. Catal.* **2015**, *326*, 69–81. [[CrossRef](#)]



92. Tom, H.W.K.; Mate, C.M.; Zhu, X.D.; Crowell, J.E.; Heinz, T.F.; Somorjai, G.A.; Shen, Y.R. Surface studies by optical second-harmonic generation: The adsorption of O<sub>2</sub>, CO, and sodium on the Rh(111) surface. *Phys. Rev. Lett.* **1984**, *52*, 348–351. [[CrossRef](#)]
93. Garfunkel, E.L.; Crowell, J.E.; Somorjai, G.A. The strong influence of potassium on the adsorption of CO on platinum surfaces. A thermal desorption spectroscopy and high-resolution electron energy loss spectroscopy study. *J. Phys. Chem.* **1982**, *86*, 310–313. [[CrossRef](#)]
94. Wang, S.J.; Yin, S.F.; Li, L.; Xu, B.Q.; Ng, C.F.; Au, C.T. Investigation on modification of Ru/CNTs catalyst for the generation of CO<sub>x</sub>-free hydrogen from ammonia. *Appl. Catal. B Environ.* **2004**, *52*, 287–299. [[CrossRef](#)]



© 2020 by the authors. Licensee MDPI, Basel, Switzerland. This article is an open access article distributed under the terms and conditions of the Creative Commons Attribution (CC BY) license (<http://creativecommons.org/licenses/by/4.0/>).